ARTICLE   OPEN

Optimized electrical control of a Si/SiGe spin qubit in the presence of an induced frequency shift

K. Takeda [1], J. Yoneda [1], T. Otsuka[1,2,3], T. Nakajima [1], M. R. Delbecq [1,4], G. Allison[1], Y. Hoshi[5], N. Usami[6], K. M. Itoh[7], S. Oda[8], T. Kodera[9] and S. Tarucha[1,10]

Electron spins confined in quantum dots are an attractive system to realize high-fidelity qubits owing to their long coherence time. With the prolonged spin coherence time, however, the control fidelity can be limited by systematic errors rather than decoherence, making characterization and suppression of their influence crucial for further improvement. Here we report that the control fidelity of Si/SiGe spin qubits can be limited by the microwave-induced frequency shift of electric dipole spin resonance and it can be improved by optimization of control pulses. As we increase the control microwave amplitude, we observe a shift of the qubit resonance frequency, in addition to the increasing Rabi frequency. We reveal that this limits control fidelity with a conventional amplitude-modulated microwave pulse below 99.8%. In order to achieve a gate fidelity >99.9%, we introduce a quadrature control method, and validate this approach experimentally by randomized benchmarking. Our finding facilitates realization of an ultra-high-fidelity qubit with electron spins in quantum dots.

INTRODUCTION

Electron spins confined in semiconductor quantum dots provide an excellent platform for scalable solid-state quantum computing.[1] Quantum operations including single-spin rotation[2–4] and two-spin entanglement control[5–7] have been realized in the past. The control fidelities for single-[8–12] and two-qubit gates[13–16] have been largely improved by recent technical advancements in extending the spin coherence time. The single-qubit control fidelities have already reached the level close to or exceeding the threshold value required for implementing fault-tolerant logical qubits in the surface code structure.[8,10–16]

As the qubit performance improves, one needs to challenge the simplified view that relates spin qubit control fidelity solely to the ratio between the dephasing rate and the operation speed, since unitary errors such as pulse-induced effects can also be relevant. This problem has never been addressed, however, for quantum-dot qubits with a single electron spin 1/2 forming a natural two-level system, in contrast to some other qubit systems where it is widely recognized (e.g. a.c. Stark shift and state leakage for transmons[17–19]). Such an approach may facilitate rapid single-qubit gates with fidelities high enough for fault-tolerant universal quantum operations,[20] where multiple single-qubit gates are commonly involved for a two-qubit gate implementation. In addition, it is also important for precise qubit error metrology based on quantum tomography, which usually relies on single-qubit control for precise state preparation and measurement.

Here we report the observation and correction of microwave pulse-induced systematic qubit errors in quantum-dot spin qubits. The spin qubit used in this work is defined in Si/SiGe quantum dots with a cobalt micro-magnet.[21] When the microwave burst is applied, in addition to the expected spin rotation, we observe an unexpected shift of the spin resonance frequency. While the frequency shift is typically an order of magnitude smaller than the Rabi frequency (f_{Rabi}), it is much larger than the spin resonance linewidth and therefore causes a systematic error in the qubit rotation axis. This will limit the single-qubit control fidelity to 99.8% according to our numerical simulations with realistic experimental parameters. To mitigate this problem and achieve high-fidelity, we introduce a quadrature microwave control which corrects the phase error of the qubit. The improvement of the qubit fidelity is experimentally confirmed by randomized benchmarking.[22]
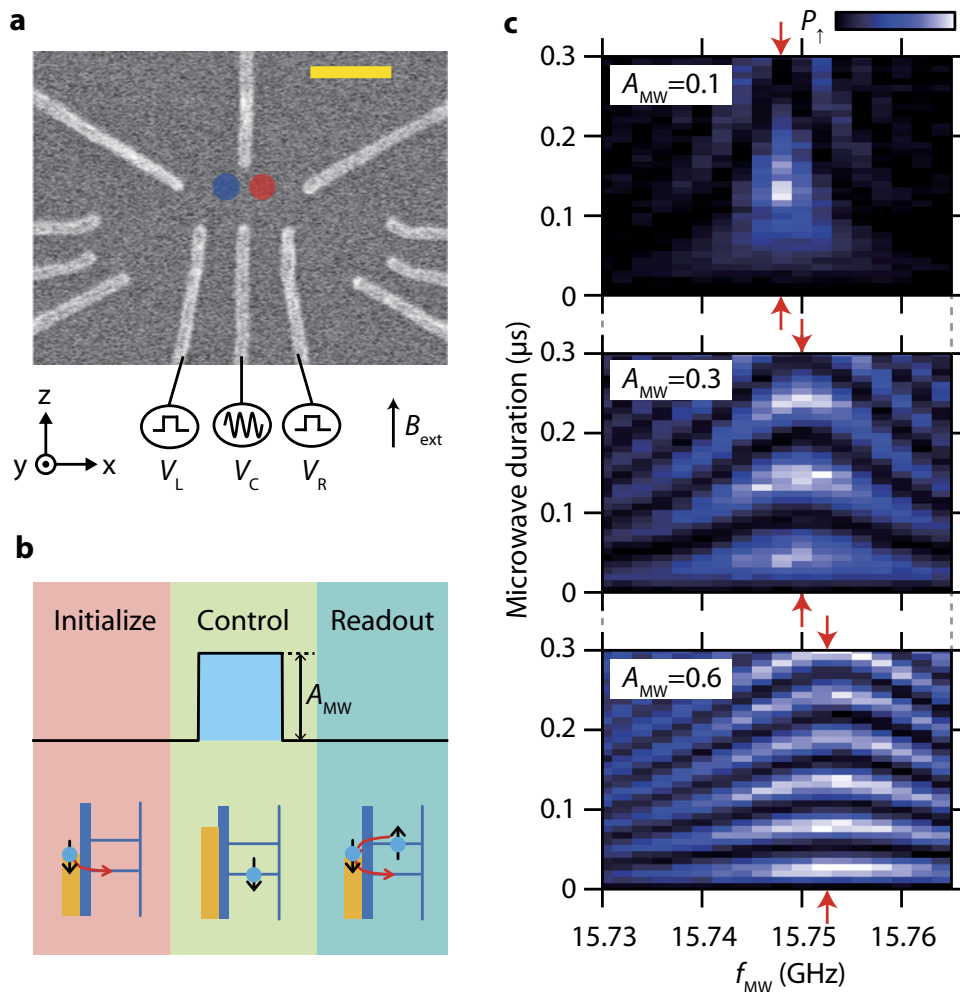
RESULTS

The quantum dots used here are formed by locally depleting a two-dimensional electron gas in an undoped Si/SiGe heterostructure using lithographically defined electrostatic gates (Fig. 1a). We measure two devices, A and B, with a nominally identical structure except for the quantum well materials to characterize sample-to-sample dependence. The quantum well in device A has a natural isotopic composition[10] and for device B it consists of isotopically enriched silicon with approximately 800 ppm ^{29}Si.[12] An on-chip

npj

Optimized electrical control of a Si/SiGe spin qubit…
K Takeda et al.

2

a

b

c

Fig. 1 Device structure and Rabi oscillation frequency shift. **a** Scanning electron microscope image of the device. The scale bar represents 200 nm. The gate electrode geometry is nominally identical for both devices A and B. Three of the gate electrodes (R, L, and C) are connected to the 50-ohm coaxial lines. The blue (red) circle shows the estimated position of the quantum dot for device A (B). **b** Pulse sequence used for the Rabi oscillation measurement. The initialization and readout are done at the same gate voltage condition where only the spin-down electron can tunnel into the dot. The compensation stage to make the pulse d.c. voltage offset to zero (used only for device A) is omitted for simplicity. **c** Rabi oscillation measured with different microwave amplitudes at $B_{ext} = 0.51$ T (device A). The red arrows show the center resonance frequency positions. As A_{MW} is increased, in addition to the increase of f_{Rabi}, the center resonance frequency increases as well

cobalt micro-magnet induces the magnetic field gradient across the quantum dot.[21] A nearby sensor quantum dot coupled to a radio-frequency tank circuit allows rapid measurement of the quantum dot charge configuration.[23] All measurements were performed at an electron temperature of approximately 120 mK (unless otherwise noted) in a dilution refrigerator with an in-plane external magnetic field B_{ext}. The spin state is read out in a single-shot manner using an energy-selective spin-to-charge conversion.[24] We use a quantum dot formed in the left (right) side of the device for device A (B). The expected lithographical dot position is shown as the blue (red) circle in Fig. 1a.

Figure 1b shows the pulse sequence for the spin control. First, a spin-down electron is prepared by applying gate voltages such that only the spin-down electron can tunnel into the dot. Next, the gate voltages are pulsed such that the electron confined in the dot is pushed deep in Coulomb blockade. Then, a microwave burst with a frequency of f_{MW} is applied to gate C to induce electric dipole spin resonance (EDSR). Finally, the gate voltages are pulsed back to the spin readout position where only a spin-up electron can tunnel out to the reservoir. When the microwave burst is applied to the gate, the electrons confined in the dot oscillate spatially in the slanting magnetic field induced by the

micro-magnet, resulting in an effective oscillating magnetic field B_{AC} perpendicular to the static magnetic field $B_0 = B_{ext} + B_z^{MM}$. At the condition where $hf_{MW} = g\mu_B B_0$ (g is the electron g-factor and μ_B is the Bohr magneton), EDSR takes place. The inhomogeneous dephasing time of each qubit is estimated to be $T_2^* \sim 1.8$ µs for device A[10] and $T_2^* \sim 20$ µs for device B[12] from the Gaussian decay of the Ramsey fringe amplitude. In addition, device A has a Hahn echo decay time $T_2^H \sim 11$ µs (the associated measurement result is available in Supplementary Section 2) and device B has a Hahn echo decay time $T_2^H \sim 99$ µs.[12]

The effect of strong EDSR microwave pulses can be readily observed in the microwave frequency dependence of the Rabi oscillations. Figure 1c shows the Rabi oscillation measured in device A with 3 different microwave amplitudes. $P_\uparrow$ is the spin-up probability obtained by averaging 500 to 1000 single-shot measurement outcomes. The applied microwave burst has a rectangular envelope with an amplitude that is denoted by $A_{MW} = 0.3\sqrt{P(f_{MW})/P_0(f_{MW})}$, where $P(f_{MW})$ is the microwave power and $P_0(f_{MW})$ is the microwave power corresponding to $f_{Rabi} = 10$ MHz. The definition results in a normalized microwave amplitude of $A_{MW} = 0.3$ at $f_{Rabi} = 10$ MHz. For the smallest microwave amplitude ($A_{MW} = 0.1$), the resonance frequency is

Optimized electrical control of a Si/SiGe spin qubit...
K Takeda et al.

npj

3
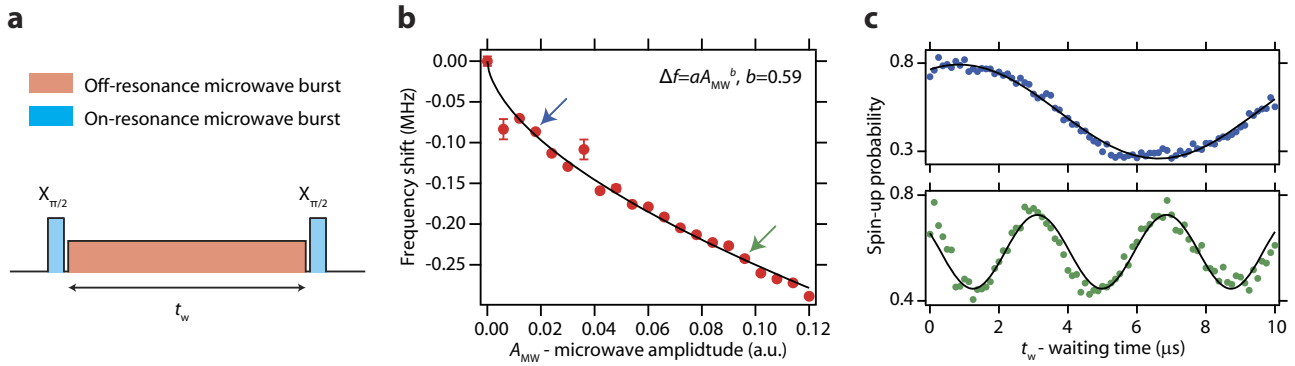
Fig. 2 Resonance frequency shift measurements (device B). **a** Schematic showing the modified Ramsey sequence. During the waiting time t_w, an off-resonance microwave burst with a rectangular envelope is applied to observe the microwave-induced frequency shift. **b** Resonance frequency shift Δf measured as a function of the off-resonance microwave amplitude A_{MW}. The red points show the experimental data and the black solid line shows a power-law fitting $\Delta f = aA_{MW}^b$ with $b = 0.59$. **c** Ramsey fringe oscillations measured under the conditions indicated by the arrows in Fig. 2b. The black solid lines show sinusoidal fitting curves
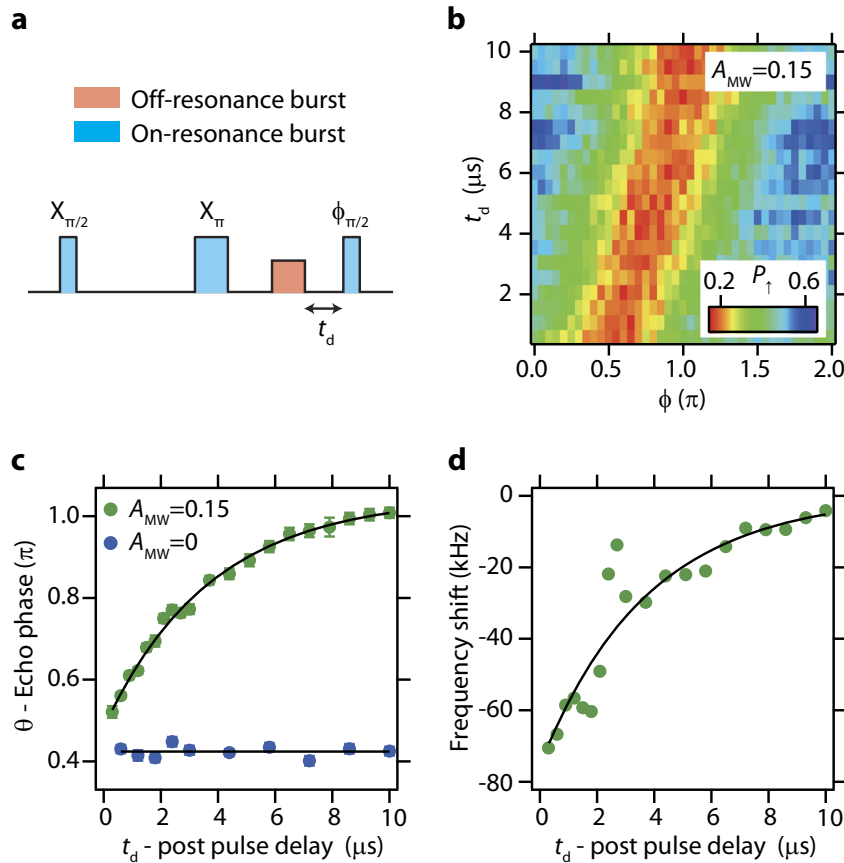

Fig. 3 Post-pulse frequency shift measurement (device B). **a** Schematic showing the modified Hahn echo sequence used to obtain the post microwave burst response. The interval between each $\pi/2$ pulse and the π pulse is fixed at 20 μs. **b** Measured echo signal shift as a function of t_d at $A_{MW} = 0.15$. **c** Extracted echo phase shift θ after turning off the microwave burst. The circles show the data obtained by fitting the echo signal with a sinusoidal function $P_\uparrow(\phi) = -E\cos(\phi + \theta(t_d)) + F$ with $E(>0)$, F, and $\theta(t_d)$ as fitting parameters. The error bars represent one standard deviation of uncertainty. The black solid lines show fitting curves. **d** Transient frequency shift derived from the echo phase accumulation at $A_{MW} = 0.15$. The black solid line shows a derivative of the exponential fitting curve $\Delta f(t_d) = (1/2\pi)(d\theta(t_d)/dt_d)$ in (**c**)

almost at the center of the image ($f_{MW} = 15.748$ GHz, indicated by the red arrows). However, when A_{MW} is increased to 0.3, the center resonance frequency moves to higher frequencies. This frequency shift is further enhanced by increasing the microwave amplitude (~ 5 MHz frequency shift for $A_{MW} = 0.6$).

To quantify the resonance frequency shift Δf more precisely, we perform a modified Ramsey interference measurement with an

off-resonance microwave burst (Fig. 2a). It is worth noting that this measurement can also check whether the shift occurs only on resonance or not. During the waiting time t_w between two resonant $X_{\pi/2}$ pulses, we apply an additional off-resonance microwave burst at a frequency of $f_{MW} = f_{res} - 180$ MHz, where $f_{res} = g\mu_B B_0/h$ is the bare qubit resonance frequency in the weak driving limit. When the qubit precession frequency shifts due to

npj
4

Optimized electrical control of a Si/SiGe spin qubit…
K Takeda et al.
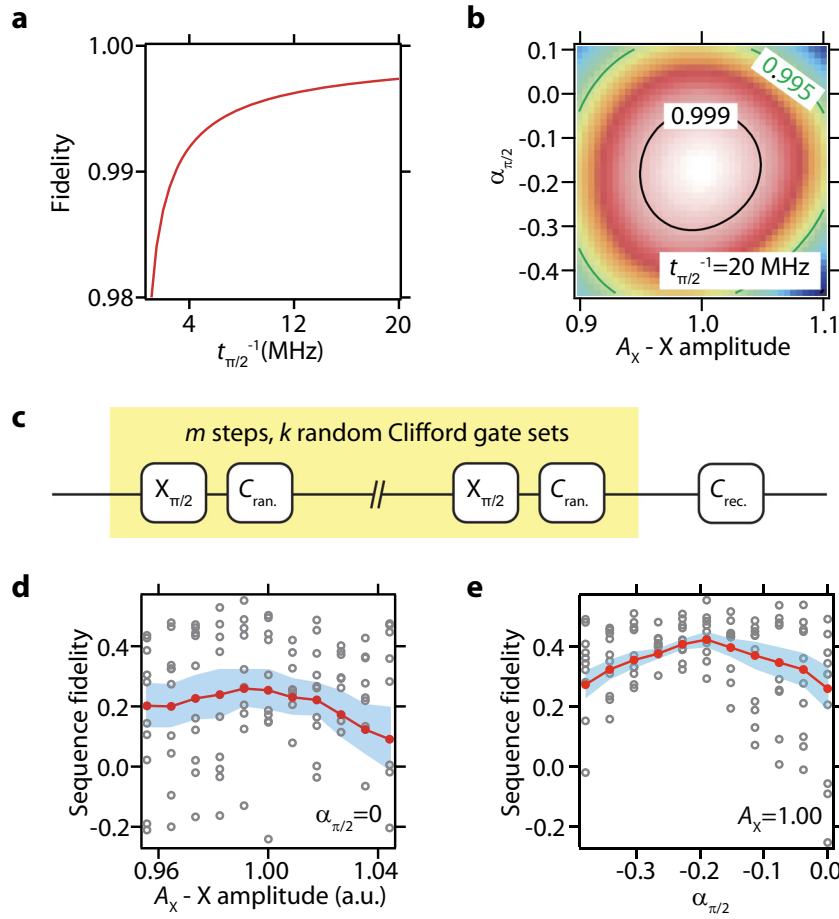
Fig. 4 Qubit fidelity analysis and optimization using a quadrature microwave control technique. **a** Calculated qubit operation clock $t_{\pi/2}^{-1}$ dependence of the averaged qubit fidelity $\bar{F}$ of $X_{\pi/2}$ gate. **b** Average qubit fidelity $\bar{F}$ as a function of the control amplitude and the quadrature control coefficient $\alpha_{\pi/2}$. The gate time is set at $t_{\pi/2} = 50$ ns. **c** Schematic showing the pulse sequence for the randomized benchmarking measurement. In between the randomly chosen Clifford gates, an $X_{\pi/2}$ gate is interleaved to characterize its fidelity. **d** Interleaved randomized benchmarking fidelity for $X_{\pi/2}$ gate measured as a function of X control amplitude A_X. A_X is directly proportional to the microwave voltage amplitude. The number of random Clifford gates is fixed at $m = 122$ and $k = 32$ gate sets are used for the measurements. The gray scattered points show the sequence fidelity for each random Clifford gate set and the red points show the sequence fidelity averaged overall 32 random gate sets. The light blue band shows standard error of the mean at each A_X. **e** Interleaved randomized benchmarking fidelity for $X_{\pi/2}$ gate measured as a function of the quadrature coefficient $\alpha_{\pi/2}$. The number of random Clifford gates is fixed at $m = 122$. The gray scattered points show the sequence fidelity for each random Clifford gate set and the red points show the sequence fidelity averaged overall 32 random gate sets. The light blue band shows standard error of the mean at each $\alpha_{\pi/2}$

the off-resonance microwave burst, the oscillation period of the Ramsey fringe changes. Figure 2b shows the frequency shift Δf for device B measured for various A_{MW}. Each data point is obtained by fitting the Ramsey oscillations using a sinusoidal function $P_\uparrow(t) = A\sin(2\pi\Delta f + \eta) + B$ with A, B, η, and Δf as fitting parameters as shown in Fig. 2c (the data for device A is available in Supplementary Section 3). We find that an empirical power-law relation $\Delta f = aA_{MW}^b$ fits well with the experimental data for both devices, however, the fitting parameters a and b are distinctively different between them. This may indicate that the frequency shift is related to some uncontrolled sample dependent parameters (e.g. local confinement potentials, defects etc.). We obtain the exponents $b = 1.39 \pm 0.02$ for device A (data shown in Fig. S3) and $b = 0.59 \pm 0.03$ for device B. Moreover, it is found that Δf is positive ($a > 0$) for device A, while it is negative ($a < 0$) for device B.

An additional striking feature of the frequency shift is observed in the post microwave burst response. We find that, even after the microwave burst is turned off, the qubit resonance frequency shift remains and causes an additional qubit phase accumulation. To quantify this, the qubit phase accumulated after a microwave burst is extracted from a Hahn echo type measurement. Here we

utilize a modified Hahn echo sequence which consists of two $\pi/2$ pulses, a π pulse, and an additional 200 ns off-resonance microwave burst (Fig. 3a). The off-resonance microwave burst is interleaved in between the π pulse and the second $\pi/2$ pulse. The phase of the second $\pi/2$ pulse is modulated by ϕ to extract the echo phase $\theta(t_d)$. The post-pulse delay time t_d indicates the time interval between the off-resonance microwave burst and the second $\pi/2$ pulse. The evolution time between the $\pi/2$ pulses and the π pulse is fixed to 20 μs to cancel out the unwanted phase fluctuation caused by quasi-static noise. Figure 3b shows the post-pulse time dependence of the echo signal. Figure 3c shows the extracted echo phase evolution after the microwave burst application. For $A_{MW} = 0$, the black solid line shows an average of the blue data points, while for $A_{MW} = 0.15$, the black solid curve shows a fitting curve with an exponential function $\theta(t_d) = C\exp(-t_d/\tau) + D$ with C, τ, and D as fitting parameters, giving a characteristic decay time of $\tau = 6$ μs. For both cases, the offset at $t_d = 0$ is mainly caused by the post-pulse phase accumulation due to the on-resonance pulses. From the measured qubit phase accumulation $\theta(t_d)$, the temporal post microwave burst frequency shift $\Delta f(t_d) = (1/2\pi)(d\theta(t_d)/dt_d)$ can be obtained (Fig. 3d). The green

Optimized electrical control of a Si/SiGe spin qubit…
K Takeda et al.

npj

5

points show numerical derivative obtained from the data points in Fig. 3c. The black solid line shows an exponential fitting curve. Although the single exponential function fits the measured phase data well for $t_d \geq 0.3$ μs, $\Delta f(t_d = 0) \sim -80$ kHz derived from the single exponential dependence extrapolation does not match the value estimated from the fitting curve to the continuous-wave response derived from Fig. 2b ($\Delta f(t_d = 0) \sim -320$ kHz with $A_{MW} = 0.15$). We also note that the similar frequency shift as observed here was also measured in a different Si/SiGe spin qubit device with micro-magnet[16] and in a phosphorous donor electron spin qubit, albeit with values several orders of magnitude smaller.[25]

There may be several physical origins for the frequency shift and among them we find that heating caused by the microwave burst may explain the exponential delayed response of the frequency shift (see Supplementary Sections 4 and 5). Since the thermal expansion is different between silicon and germanium, the increase of the lattice temperature can cause a change of the strain in the quantum well.[26] The strain caused by the metallic gate electrodes[27] may also be temperature dependent. In any case, the strain variation modifies the potential shape for the confined electron and the center quantum dot position. Because of the magnetic field gradient, the quantum dot position shift results in the local magnetic field or the resonance frequency shift. Since it takes some time to cool down the system to the base temperature after turning off the microwave burst, the frequency shift occurs during and even after the microwave burst application. However, this does not explain the discontinuous frequency shift between the continuous-wave response in Fig. 2b and the exponential decay in Fig. 3c because there should be no abrupt change in the system temperature before and after turning off the microwave burst. Although the detailed physical mechanism will not affect the qubit fidelity optimization described in what follows, further investigation is needed to fully explain the observed frequency shift.

Now we turn to the qubit control fidelity. The observed resonance frequency shift affects the control fidelity because it is much larger than the fluctuation of resonance frequency for our device ($\sigma \sim 20.6$ kHz for device B). Therefore, here we discuss the qubit control optimization in the presence of such a microwave amplitude dependent frequency shift. The simplest way to cancel the frequency shift effect may be to keep the microwave amplitude always constant by applying off-resonance microwave even when the qubit is idle.[16] In this way, the qubit frequency shift during the control stage is kept constant and we can choose the shifted qubit resonance frequency as the rotating frame frequency. However, this method causes too much additional heating of the device which may be harmful for the qubit control because we need a relatively large microwave power to realize the qubit rotation faster than the dephasing time. In addition, due to the limited bandwidth of the microwave modulation circuit, creation of the smooth shaped pulse is difficult for this type of control including abrupt frequency switching.

We therefore investigate a way to cancel out the unwanted qubit phase accumulation by quadrature microwave control.[17,19,28] The technique was originally proposed for canceling the microwave-induced frequency shift (a.c. Stark shift) and the state leakage of transmon qubits. Because spin qubits generally have a well-defined two-level system and the state leakage is negligible, the quadrature control can be used to just correct the microwave-induced frequency shifts. In this case, in contrast to the transmon qubit case where the single quadrature parameter has to be set to an optimal point to balance the compensation of two infidelity sources, one quadrature parameter can be used to fully compensate the influence of the frequency shift. To calculate the single-qubit time evolution, here we consider the rotating frame Hamiltonian of the system written as follows:

$$-2\hbar^{-1}H(t) = X(t)\sigma_x + Y(t)\sigma_y + Z(t)\sigma_z, \qquad (1)$$

where $X(t)$ and $Y(t)$ are the EDSR microwave control amplitudes, $Z(t)$ is the frequency shift caused by the XY control, and $\hbar$ is the reduced Planck's constant. The rotating frame frequency and f_{MW} are set at the qubit resonance frequency during the free evolution with $X(t) = Y(t) = 0$. Here we consider the pulse optimization for a Gaussian $\pi/2$ rotation $X(t) = A_X \exp(-t^2/2\sigma^2)$ and the quadrature derivative control $Y(t) = a_{\pi/2}\sigma(dX(t)/dt)$ truncated at $\pm 2\sigma$. A_X is the microwave control amplitude normalized with the ideal $\pi/2$ control amplitude $A_{\pi/2} = \pi / \left(\sigma \int_{-2}^{2} \exp(-t^2/2)dt \right)$. Note that the quadrature coefficient a has to be adjusted independently for π and $\pi/2$ pulses. The microwave-induced frequency shift is calculated from the power-law relation $Z(t) = a(X(t)^2 + Y(t)^2)^{b/2}$ ($t \in [-2\sigma, 2\sigma]$), i.e. it is assumed to be dominated by the instantaneous response and the slowly changing part is ignored. The partial optimization still works reasonably well to mitigate the qubit control errors because the slow delayed response is several times smaller than the fast response.

Figure 4a shows a plot of the averaged qubit control fidelity $\bar{F}$ of $X_{\pi/2}$ gate calculated using the equation $\bar{F}(U, \mathcal{E}) = 1/2 + (1/12) \sum_j \text{Tr}(U\sigma_j U^\dagger \mathcal{E}\sigma_j)$, where $U = \exp(i\pi\sigma_x/4)$ is the ideal process matrix and $\mathcal{E}$ is the actual quantum operation.[29] Here we plot $\bar{F}$ for the gate clock frequency $t_{\pi/2}^{-1} = 1/4\sigma$ ranging from 1 to 20 MHz, which is a reasonable operation range for device B. In this qubit operation range, $\bar{F}$ is limited to approximately 99.8% because of the unwanted phase accumulation due to the frequency shift. In Fig. 4b, we calculate $\bar{F}$ at $t_{\pi/2}^{-1} = 20$ MHz (corresponds to $f_{Rabi} = 5$ MHz for rectangular microwave burst) as a function of $\pi/2$ quadrature coefficient $a_{\pi/2}$. The model predicts a gate fidelity higher than 99.999% with an optimized parameter set at $A_X = 1.00$ and $a_{\pi/2} = -0.173$. (The graphical Bloch sphere representation of the qubit evolution is depicted in Fig. S6). We experimentally confirm the effectiveness of the quadrature control using an interleaved randomized benchmarking technique (Fig. 4c). Only device B is used for this measurement as the influence of the frequency shift is too subtle to observe experimentally in device A. The $X_{\pi/2}$ interleaved randomized benchmarking is used to characterize the fidelity of $X_{\pi/2}$ gate and f_{MW} is set to the free evolution frequency calibrated by the Ramsey fringe. Figure 4d, e show the $X_{\pi/2}$ interleaved randomized benchmarking sequence fidelity F at a fixed number of Clifford gates, $m = 122$, measured for various values of $a_{\pi/2}$ and A_X. The sequence fidelity is defined as $F = P_\uparrow^{|\uparrow\rangle} - P_\uparrow^{|\downarrow\rangle}$, where $P_\uparrow^{|\uparrow\rangle}(P_\uparrow^{|\downarrow\rangle})$ is the measured spin-up probability for the sequence designed to obtain $|\uparrow\rangle(|\downarrow\rangle)$ as an ideal final state. To clarify the parameter dependence of $a_{\pi/2}$ and A_X, the other parameters (microwave frequency and amplitude, a for other Clifford gates) are adjusted to maximize the sequence fidelity. We find that the sequence fidelity is maximized at $a_{\pi/2} = -0.18$, which is in reasonable agreement with the value derived from the theory. The small deviation may come from the post-pulse effect. From a separate measurement using the same device and the quadrature control, we obtain a single gate fidelity as high as 99.93 %[12] and this is well above the upper limit given by the microwave burst induced frequency shift.

DISCUSSION

We have reported the shift of resonance frequency of electron spin qubits in Si/SiGe quantum dots with increasing applied microwave burst amplitude and quadrature control method to cancel out the qubit control error cause by the frequency shift. Although part of the observed frequency shift may be explained by the effect of heating, the overall physical origin remains unknown and full characterization needs further investigation. Nevertheless, for the purpose of practical optimization of quadrature compensation pulse presented in this work, the Ramsey-based measurement of the amplitude dependence described in Fig. 2 is sufficient. We anticipate that the full understanding of the frequency shift mechanism will allow for

Optimized electrical control of a Si/SiGe spin qubit…
K Takeda et al.

6

further optimizations beyond what is presented in this work, such as the prediction of the frequency shift from the device parameters and the minimization of the frequency shift itself by the device design.

METHODS

In both devices, the quantum dot is formed by locally depleting the two-dimensional electron gas in an undoped Si/SiGe heterostructure. A 250 nm thick cobalt micro-magnet is deposited on top of the accumulation gate to induce a stray magnetic field across the quantum dot. The sample is cooled down using a dilution refrigerator to a base electron temperature of approximately 120 mK (unless otherwise noted) which is estimated from the transport linewidth. Further details about the devices and the measurement setup are described in Supplementary information, ref. [10] (device A), and [12] (device B).

For both devices, the valley splitting is confirmed by magneto-spectroscopy measurement to be larger than the Zeeman splitting. Therefore, the physics in this work is mainly described by a conventional single-valley picture, although there may be a small fraction of the population in the excited valley state due to initialization errors.

DATA AVAILABILITY

The data that support the findings of this study are available from the corresponding author upon reasonable request.

AUTHOR CONTRIBUTIONS

K.T. and J.Y. performed the measurements and analyzed the data. K.T. and T.O. fabricated the samples. Y. H., N. U., and K. M. I. supplied the isotopically enriched Si/SiGe heterostructure. K.T. wrote the article with inputs from the rest of the authors. M. R.D., G.A., T.N., S.O., and T.K. contributed to the sample fabrication, measurement, and data analysis. S.T. supervised the project.

ADDITIONAL INFORMATION

Supplementary information accompanies the paper on the *npj Quantum Information* website (https://doi.org/10.1038/s41534-018-0105-z).

Competing interests: The authors declare no competing interests.

Publisher's note: Springer Nature remains neutral with regard to jurisdictional claims in published maps and institutional affiliations.

REFERENCES

1. Loss, D. & DiVincenzo, D. P. Quantum computation with quantum dots. *Phys. Rev. A* **57**, 120 (1998).
2. Koppens, F. H. L. et al. Driven coherent oscillations of a single electron spin in a quantum dot. *Nature* **442**, 766–771 (2006).
3. Nowack, K. C., Koppens, F. H. L., Nazarov, Y. V. & Vandersypen, L. M. K. Coherent control of a single electron spin with electric fields. *Science* **318**, 1430–1433 (2007).
4. Pioro-Ladriere, M. et al. Electrically driven single-electron spin resonance in a slanting Zeeman field. *Nat. Phys.* **4**, 776–779 (2008).
5. Brunner, R. et al. Two-qubit gate of combined single-spin rotation and interdot spin exchange in a double quantum dot. *Phys. Rev. Lett.* **107**, 146801 (2011).
6. Petta, J. R. et al. Coherent manipulation of coupled electron spins in semi-conductor quantum dots. *Science* **309**, 2180–2184 (2005).
7. Shulman, M. D. et al. Demonstration of entanglement of electrostatically coupled singlet-triplet qubits. *Science* **336**, 202–205 (2012).
8. Veldhorst, M. et al. An addressable quantum dot qubit with fault-tolerant control fidelity. *Nat. Nanotechnol.* **9**, 981–985 (2014).
9. Eng, K. et al. Isotopically enhanced triple-quantum-dot qubit. *Sci. Adv.* **1**, e1500214 (2015).
10. Takeda, K. et al. A fault-tolerant addressable spin qubit in a natural silicon quantum dot. *Sci. Adv.* **2**, e1600694 (2016).
11. Kawakami, E. et al. Gate fidelity and coherence of an electron spin in a Si/SiGe quantum dot with micro-magnet. *Proc. Natl Acad. Sci.* **113**, 11738–11743 (2016).
12. Yoneda, J. et al. A quantum-dot spin qubit with coherence limited by charge noise and fidelity higher than 99.9%. *Nat. Nanotechnol.* **13**, 102–106 (2018).
13. Veldhorst, M. et al. A two-qubit logic gate in silicon. *Nature* **526**, 410–414 (2015).
14. Nichol, J. M. et al. High-fidelity entangling gate for double-quantum-dot spin qubits. *npj Quantum Inf.* **3**, 3 (2017).
15. Zajac, D. M. et al. Resonantly driven CNOT gate for electron spins. *Science* **359**, 439–442 (2018).
16. Watson, T. F. et al. A programmable two-qubit quantum processor in silicon. *Nature* **555**, 633–637 (2018).
17. Lucero, E. et al. Reduced phase error through optimized control of a super-conducting qubit. *Phys. Rev. A* **82**, 042339 (2010).
18. Chow, J. M. et al. Optimized driving of superconducting artificial atoms for improved single-qubit gates. *Phys. Rev. A* **82**, 040305(R) (2009).
19. Chen, Z. et al. Measuring and Suppressing Quantum State Leakage in a Super-conducting Qubit. *Phys. Rev. Lett.* **116**, 020501 (2016).
20. Fowler, A. G., Stephens, A. M. & Groszkowski, P. High-threshold universal quan-tum computation on the surface code. *Phys. Rev. A* **80**, 052312 (2009).
21. Tokura, Y., Van Der Wiel, W. G., Obata, T. & Tarucha, S. Coherent single electron spin control in a slanting Zeeman field. *Phys. Rev. Lett.* **96**, 047202 (2006).
22. Knill, E. et al. Randomized benchmarking of quantum gates. *Phys. Rev. A* **77**, 012307 (2008).
23. Reilly, D. J., Marcus, C. M., Hanson, M. P. & Gossard, A. C. Fast single-charge sensing with a rf quantum point contact. *Appl. Phys. Lett.* **91**, 162101 (2007).
24. Elzerman, J. M. et al. Single-shot read-out of an individual electron spin in a quantum dot. *Nature* **430**, 431–435 (2004).
25. Freer, S. et al. A single-atom quantum memory in silicon. *Quantum Sci. Technol.* **2**, 015009 (2017).
26. Park, J. et al. Electrode-stress-induced nanoscale disorder in Si quantum elec-tronic devices. *APL Mater.* **4**, 066102 (2016).
27. Popescu, D. P., Eliseev, P. G., Stintz, A. & Malloy, K. J. Temperature dependence of the photoluminescence emission from InAs quantum dots in a strained $Ga_{0.85}In_{0.15}As$ quantum well. *Semicond. Sci. Technol.* **19**, 33–38 (2004).
28. Motzoi, F., Gambetta, J. M., Rebentrost, P. & Wilhelm, F. K. Simple pulses for elimination of leakage in weakly nonlinear Qubits. *Phys. Rev. Lett.* **103**, 110501 (2009).
29. Nielsen, M. A. A simple formula for the average gate fidelity of a quantum dynamical operation. *Phys. Lett. A* **303**, 249–252 (2002).